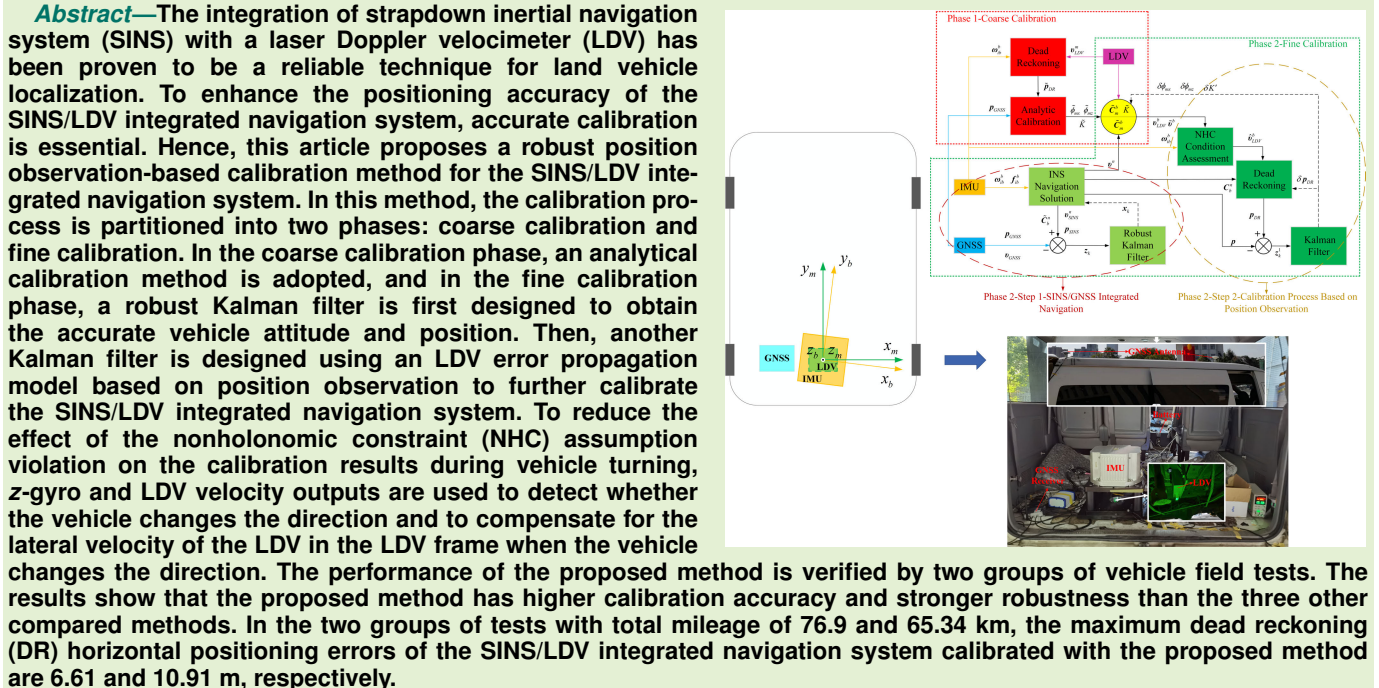


# A Robust Online Calibration Method for SINS/LDV Integrated Navigation System Based on Position Observation

Zhiyi Xiang<sup>ID</sup>, Qi Wang, Rong Huang<sup>ID</sup>, Shilong Jin<sup>ID</sup>, Xiaoming Nie<sup>ID</sup>, and Jian Zhou<sup>ID</sup>



**Index Terms**—Calibration, laser Doppler velocimeter (LDV), position observation, strapdown inertial navigation system (SINS).

## I. INTRODUCTION

S TRAPDOWN inertial navigation system (SINS) is widely used in autonomous land navigation because it can output multiple navigation parameters, operates independently, has a high output frequency, and is well concealed. However, the SINS error accumulates over time, which is not conducive to

Manuscript received 3 October 2023; accepted 14 November 2023. Date of publication 23 November 2023; date of current version 2 January 2024. This work was supported in part by the Major Basic Autonomous Research Project of the College of Advanced Interdisciplinary Studies, National University of Defense Technology, under Grant ZDJC19-12; and in part by the Natural Science Foundation of Hunan Province, China, under Grant 2021JJ30782. The associate editor coordinating the review of this article and approving it for publication was Dr. Baoding Zhou. (*Corresponding author: Jian Zhou.*)

The authors are with the Nanhua Laser Laboratory, College of Advanced Interdisciplinary Studies, National University of Defense Technology, Changsha 410073, China (e-mail: wttzhoujian@163.com).

Digital Object Identifier 10.1109/JSEN.2023.3333898

long-term high-precision navigation [1]. Therefore, integrated navigation technology has become a popular research area. Global navigation satellite systems (GNSSs) have been widely used to reduce the error accumulation of SINS. However, when land vehicles travel between tall buildings or in areas with tree cover or tunnels, GNSS may encounter frequent signal occlusion or even interruption, leading to divergence of integrated navigation results [2], [3]. The odometer (OD) can provide velocity and position increment information for a vehicle by sensing the rotation of its wheel axle [4]. As a result, the OD is fully autonomous and most current research on autonomous navigation methods for land vehicles in GNSS-denied scenarios focuses on SINS/OD integrated navigation. Although many studies have demonstrated the superior performance of the SINS/OD integrated navigation system, the influence of vehicle tire condition and driving condition on the OD is unavoidable. This limits the positioning accuracy

of the SINS/OD integrated navigation system in practical applications [5], [6], [7], [8], [9], [10].

Laser Doppler velocimeter (LDV) is an instrument based on laser scattering that uses the Doppler frequency shift of scattered light from moving particles to determine the velocity of particles [11]. It has the characteristics of noncontact measurement, high accuracy of velocimetry, a wide range of velocimetry, good dynamic performance, good autonomy, and good real-time performance [12]. The noncontact measurement characteristic of LDV makes the measurement value of onboard LDV independent of the tire state of the vehicle. As a result, LDV is more suitable for measuring the velocity information of land vehicles than OD. In addition, LDV theoretically has better real-time performance than OD because it directly measures the velocity of the vehicle rather than its position increment. In recent years, LDV has been used for terrestrial navigation and integrated with SINS. Many studies have shown the effectiveness of this integration [13], [14], [15], [16], [17], [18], [19].

The nonholonomic constraint (NHC) is widely used in SINS/OD integrated navigation systems. It is based on the assumption that no slippage or jump occurs during vehicle driving, meaning that both the lateral and vertical velocities of the vehicle are zero. By combining the forward velocity of the vehicle obtained from OD measurements with NHC, the 3-D velocity of the vehicle can be obtained. Since both 1-D LDV (1D-LDV) and OD are used to measure the forward velocity of a vehicle, the SINS/LDV integrated navigation system shares many similarities with the SINS/OD integrated navigation system, i.e., installation misalignment angle, lever arm error, and sensor's own scale factor error are also present in the SINS/LDV integrated navigation system. Among them, the installation misalignment angle of the LDV is caused by the noncoincidence between the body frame where the inertial measurement unit (IMU) is located and the LDV frame, the scale factor error of the LDV is caused by the difference between the actual and design values of the LDV beam inclination angle, and the lever arm error is caused by the deviation between the IMU installation point and the effective point of the NHC.

Yan [20] pointed out that if the pitch and heading installation misalignment angles are not calibrated, they will significantly influence the positioning accuracy of the SINS/OD integrated navigation system for long-range navigation applications. Therefore, in order to improve the accuracy of the SINS/LDV integrated navigation system, it is necessary to accurately calibrate the installation deviation between the LDV frame and the body frame, the scale factor error of LDV, and the lever arm error between IMU and LDV. In particular, the installation deviation between the LDV frame and the body frame and the scale factor error of LDV are especially important.

The online calibration method based on Kalman filter is the most common calibration method in the integrated navigation system [21], [22], [23], [24], [25], [26], [27], [28], [29]. Wu et al. [21] used the OD output and the NHC as velocity updates to calibrate the attitude misalignment angle, the lever arm error, and the scale factor error of OD for the SINS/OD integrated navigation system. They also conducted

a rigorous observability analysis of the error terms. Wang et al. [22], [24] applied this approach to accurately calibrate the SINS/2D-LDV and SINS/3D-LDV integrated navigation systems. Zhu et al. [25] replaced differenced GNSS (DGNSS) or precise point positioning techniques with time-differenced carrier phase observations to complete the calibration process of the SINS/1D-LDV integrated navigation system. The trajectory similarity principle is also used to calibrate the onboard navigation system. Yan [20] calibrated the scale factor error of OD and the pitch and heading installation misalignment angles of IMU and OD using the similarity principle between the dead reckoning (DR) trajectory and the true trajectory. Gao et al. [30] followed this idea and used the GNSS trajectory and the SINS/LDV DR trajectory of the first few minutes after initial alignment to perform a coarse calibration process. They used the coarse calibration result as the initial value for the subsequent filter calibration to improve the calibration accuracy. Considering that GNSS is not always reliable, Xi et al. [31] used highly accurate output information in the early stage of the inertial navigation system to obtain the scale factor of LDV and the heading installation error angle of the SINS/1D-LDV integrated navigation system. Some optimal estimation methods other than Kalman filtering are also used for calibrating an integrated navigation system [32], [33], [34], [35], [36]. Zhang et al. [33] proposed an independent calibration method for the SINS/LDV integrated navigation system that uses the least squares algorithm and does not depend on any additional equipment or benchmarks. Xiang et al. [34] used Davenport's q-method to estimate the misalignment angle matrix of the SINS/LDV integrated navigation system.

Currently, the NHC-based velocity observation method is the predominant calibration method for integrated navigation systems. However, if the vehicle no longer conforms to the NHC, the calibration effect of such methods will be greatly reduced. In addition, although velocity observation is more accurate and robust than acceleration observation, it is still susceptible to noise and outliers. To ensure the calibration accuracy of the SINS/LDV integrated navigation system in a nonideal environment, we proposed a calibration method based on position observation in our previous work [34]. However, this method has a limitation: the position observation is obtained by summing up the position increments for each time period, which leads to a continuous decrease in the accuracy of its position observation due to the accumulation of position increment errors. Therefore, a more robust and accurate position observation-based calibration method for the SINS/LDV integrated navigation system is proposed in this article. Compared with previous calibration methods for the SINS/LDV integrated navigation system, the main contributions of this article are given as follows: 1) a Kalman filter is designed using an LDV error propagation model based on position observation to calibrate the SINS/LDV integrated navigation system; 2) a robust Kalman filter is designed to obtain the SINS/GNSS integrated navigation results and reduce the influence of GNSS outliers on them; and 3) a method is introduced to detect whether the vehicle changes the direction according to z-gyro and LDV velocity outputs and

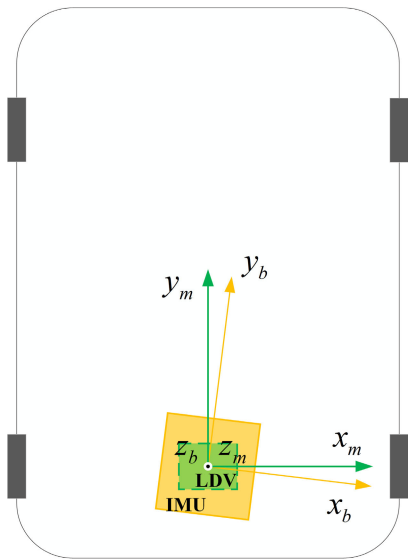


Fig. 1. Installation relationship between the IMU and the LDV.

to compensate for the lateral velocity of the LDV in the LDV frame when the vehicle changes the direction to reduce the effect of violating the NHC on the calibration results during vehicle turning.

The rest of this article is organized as follows. In Section II, the calibration parameters in SINS/LDV integrated navigation system are introduced. In Section III, a robust position observation-based calibration method for the SINS/LDV integrated navigation system is proposed. In Section IV, the proposed calibration method is compared with the traditional calibration method by using the vehicle-mounted field test data from an LDV-aided SINS. Concluding remarks are given in Section V.

## II. CALIBRATION PARAMETERS IN SINS/LDV INTEGRATED NAVIGATION SYSTEM

The installation relationship between the IMU and the LDV is shown in Fig. 1. The LDV frame (*m* frame) is defined as right-forward-upward, while the IMU body frame (*b* frame) is also defined as right-forward-upward. The navigation frame (*n* frame) is defined as east-north-up.

The 1-D velocity along the vehicle trajectory, provided by the 1D-LDV, and the well-known NHC of land vehicles can be used to achieve 3-D velocity measurements of land vehicles. Denoting the true travel speed of the vehicle by  $v_y$ , the true velocity of the vehicle in the *m* frame can be expressed as

$$\mathbf{v}^m = [0 \quad v_y \quad 0]^T. \quad (1)$$

The LDV measures the velocity accurately by sensing the Doppler frequency shift of backscattered light. Fig. 2 shows the optical path structure of a traditional 1D-LDV system.  $\theta$  is the incident angle of the beam.  $v_{LDV}$  denotes the velocity of a 1D-LDV, as given by the following equation:

$$v_{LDV} = \lambda f_D / (2 \cos \theta) = K f_D = v_y \quad (2)$$

where  $\lambda$  denotes the wavelength of the laser,  $f_D$  is the Doppler frequency, and  $K$  denotes the scale factor of the LDV.

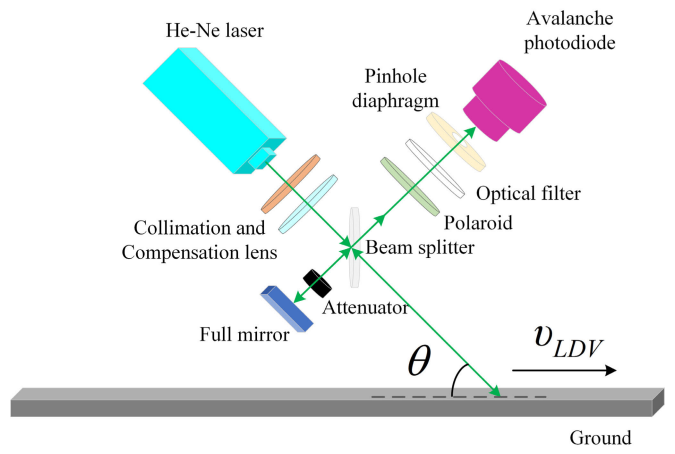


Fig. 2. Optical schematic of the traditional 1D-LDV.

Equation (2) shows that the scale factor of LDV depends on the wavelength of the laser and the beam inclination angle of LDV. However, in practical applications, these parameters may deviate from their true values, which will lead to the scale factor error. Therefore, the vehicle velocity measured by LDV in the *m* frame is

$$\begin{aligned} \mathbf{v}_{LDV}^m &= [0 \quad \tilde{v}_{LDV} \quad 0]^T = [0 \quad (1 + \delta K)v_{LDV} \quad 0]^T \\ &= (1 + \delta K)\mathbf{v}^m \end{aligned} \quad (3)$$

where  $\delta K$  denotes the scale factor error and  $\tilde{v}_{LDV}$  is the actual output of a 1D-LDV.

As shown in Fig. 1, due to the constraints of the installation conditions, it is difficult for the *m* frame to be aligned with the *b* frame, resulting in angular misalignment between the two frames. The installation misalignment angles between the *m* frame and the *b* frame can be expressed by a vector,  $\boldsymbol{\phi}_m = [\phi_{mx} \quad \phi_{my} \quad \phi_{mz}]^T$ , where  $\phi_{mx}$ ,  $\phi_{my}$ , and  $\phi_{mz}$  denote the pitch installation misalignment angle, the roll installation misalignment angle, and the heading installation misalignment angle, respectively. Since the installation misalignment angle is usually very small, the transformation matrix from the *m* frame to the *b* frame can be approximated as

$$\mathbf{C}_m^b = \mathbf{I}_3 - \boldsymbol{\phi}_m \times = \begin{bmatrix} 1 & \phi_{mz} & -\phi_{my} \\ -\phi_{mz} & 1 & \phi_{mx} \\ \phi_{my} & -\phi_{mx} & 1 \end{bmatrix} \quad (4)$$

where  $\mathbf{I}_3$  is the  $3 \times 3$  identity matrix and  $\boldsymbol{\phi}_m \times$  denotes the antisymmetric matrix of  $\boldsymbol{\phi}_m$ .

According to (4), the velocity of the LDV in the *b* frame can be calculated as

$$\mathbf{v}_{LDV}^b = \mathbf{C}_m^b \mathbf{v}_{LDV}^m = [\phi_{mz} \tilde{v}_{LDV} \quad \tilde{v}_{LDV} \quad -\phi_{mx} \tilde{v}_{LDV}]^T. \quad (5)$$

It is worth noting that the effect of the lever arm is not considered in the traditional SINS/LDV integrated calibration methods because, unlike the OD, the LDV can be easily mounted alongside the IMU. In addition, (5) shows that for 1D-LDV, the roll installation misalignment angle has no effect on the velocity of the LDV in both the *b* and *n* frames. Therefore, it is unobservable and should be disregarded.

In the  $n$  frame, the attitude error of SINS satisfies

$$\tilde{\mathbf{C}}_b^n = (\mathbf{I}_3 - \boldsymbol{\varphi} \times) \mathbf{C}_b^n \quad (6)$$

where  $\mathbf{C}_b^n$  and  $\tilde{\mathbf{C}}_b^n$  are the true and error-contaminated attitude matrices from the  $b$  frame to the  $n$  frame, respectively, and  $\boldsymbol{\varphi}$  and  $\boldsymbol{\varphi} \times$  denote the attitude error of SINS and its corresponding antisymmetric matrix, respectively.

Since the velocity of the vehicle measured by the LDV in the  $n$  frame depends on the attitude output of the SINS, the velocity of the LDV in the  $n$  frame will be affected by the attitude error of the SINS. Therefore, the velocity of the LDV in the  $n$  frame can be expressed as

$$\mathbf{v}_{\text{LDV}}^n = \tilde{\mathbf{C}}_b^n \mathbf{C}_m^b \mathbf{v}_{\text{LDV}}^m = (\mathbf{I}_3 - \boldsymbol{\varphi} \times) \mathbf{C}_b^n \mathbf{C}_m^b \mathbf{v}_{\text{LDV}}^m. \quad (7)$$

According to (3), (5), and (7), the velocity error of the LDV in the  $n$  frame can be derived as

$$\begin{aligned} \delta \mathbf{v}_{\text{LDV}}^n &= \mathbf{v}_{\text{LDV}}^n - \mathbf{v}^n \\ &= (\mathbf{I}_3 - \boldsymbol{\varphi} \times) \mathbf{C}_b^n (\mathbf{I}_3 - \boldsymbol{\phi}_m \times) (1 + \delta K) \mathbf{v}^m - \mathbf{v}^n \\ &\approx (\mathbf{v}^n \times) \boldsymbol{\varphi} + \mathbf{C}_b^n (\mathbf{v}^m \times) \boldsymbol{\phi}_m + \delta K \mathbf{v}^n \end{aligned} \quad (8)$$

where  $\mathbf{v}^n$  denotes the vehicle true velocity in the  $n$  frame.

### III. PROPOSED CALIBRATION METHOD FOR SINS/LDV INTEGRATED NAVIGATION SYSTEM

Fig. 3 shows the overall block diagram of the proposed calibration method for the SINS/LDV integrated navigation system based on position observation. The method consists of two separate phases: phase 1 performs the coarse calibration using the analytical method and phase 2 performs the fine calibration using the filtering method. Phase 2 consists of two independent steps. In the first step, the SINS/GNSS integrated navigation process is performed to obtain accurate attitude, velocity, and position information of the vehicle. A robust Kalman filter is used for the SINS/GNSS integrated navigation process to reduce the effect of GNSS outliers. In the second step of phase 2, the output velocity of the LDV is corrected using the calibration parameters obtained from the coarse calibration process. The DR process is then executed based on the vehicle attitude information obtained in the first step. A Kalman filter, designed using the LDV error propagation model based on position observation, is employed to achieve the accurate calibration of the SINS/LDV integrated navigation system. Considering that the NHC of the vehicle may be disrupted during turning, judgment conditions for violating NHC are established based on the output of the LDV and the output of the  $z$ -axis gyro of the IMU. When NHC is violated, lateral velocity compensation is performed for the velocity of the LDV in the  $m$  frame, according to the projection of the SINS/GNSS velocity in the  $m$  frame.

#### A. Coarse Calibration Process

Gao et al. [30] proposed an analytical calibration method based on the trajectory similarity principle and applied it to the coarse calibration process of the SINS/LDV integrated navigation system. However, this method does not consider the pitch installation misalignment angle. As shown in (5), the pitch installation misalignment angle affects the vertical velocity of

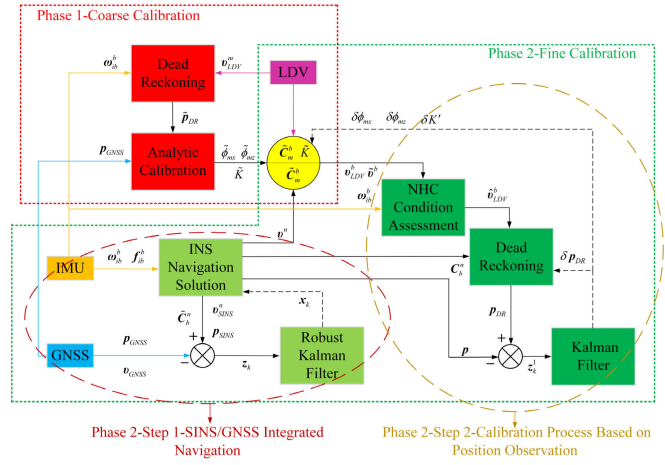


Fig. 3. Block diagram of the proposed calibration method.

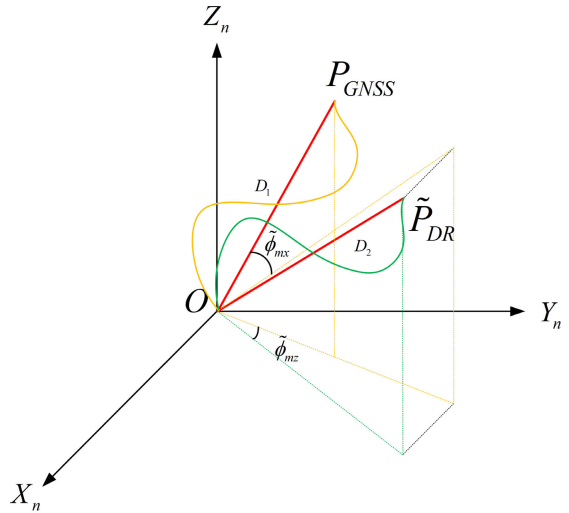


Fig. 4. Schematic of the relationship between GNSS trajectory and DR trajectory.

the LDV in the  $b$  frame, which in turn influences the estimation of the vehicle height. In this section, the analytical calibration method proposed in [30] is extended from 2-D to 3-D based on the principle of trajectory similarity. This allows for the determination of coarse calibration results for not only the LDV scale factor and heading installation misalignment angle but also for the pitch installation misalignment angle. Fig. 4 shows the relationship between the GNSS trajectory and the SINS/LDV DR trajectory at the initial time in the  $n$  frame. Point  $O$  indicates the initial position of the vehicle, and its coordinate is  $(X_O, Y_O, Z_O)$ . Points  $P_{\text{GNSS}}$  and  $\tilde{P}_{\text{DR}}$  denote the positions of the vehicle after a short period of motion, as obtained by GNSS and SINS/LDV DR, respectively. Their coordinates are  $(X_{\text{GNSS}}, Y_{\text{GNSS}}, Z_{\text{GNSS}})$  and  $(X_{\text{DR}}, Y_{\text{DR}}, Z_{\text{DR}})$ , respectively.  $D_1$  and  $D_2$  are the distances from  $O$  to  $P_{\text{GNSS}}$  and from  $O$  to  $\tilde{P}_{\text{DR}}$ , respectively.

According to Fig. 4, the coarse calibration results for both the scale factor and the installation misalignment angles are

$$\tilde{K} = \frac{D_1}{D_2} \quad (9)$$

$$\tilde{\phi}_{mx} = a \sin\left(\frac{Z_{\text{GNSS}} - Z_O}{D_1}\right) - a \sin\left(\frac{Z_{\text{DR}} - Z_O}{D_2}\right) \quad (10)$$

$$\tilde{\phi}_{mz} = a \tan\left(\frac{Y_{\text{GNSS}} - Y_O}{X_{\text{GNSS}} - X_O}\right) - a \tan\left(\frac{Y_{\text{DR}} - Y_O}{X_{\text{DR}} - X_O}\right). \quad (11)$$

After completing the coarse calibration, the parameters obtained are used as initial values for the subsequent fine calibration process.

### B. Fine Calibration Process

This section proposes a robust fine calibration method for the SINS/LDV integrated navigation system to ensure its calibration accuracy in a nonideal environment. The method consists of two parts: SINS/GNSS integrated navigation and filtering calibration based on position observation. These parts are described in detail next.

**1) SINS/GNSS Integrated Navigation:** For the SINS/GNSS integrated navigation system, the error model of SINS is given by

$$\begin{aligned} \dot{\boldsymbol{\varphi}} &= \boldsymbol{\varphi} \times \boldsymbol{\omega}_{in}^n + \delta \boldsymbol{\omega}_{in}^n - \mathbf{C}_b^n \boldsymbol{\epsilon}_{ib}^b \\ \delta \dot{\mathbf{v}}_{\text{SINS}}^n &= -\boldsymbol{\varphi} \times \mathbf{f}^n + \delta \mathbf{v}_{\text{SINS}}^n \times (2\boldsymbol{\omega}_{ie}^n + \boldsymbol{\omega}_{en}^n) \\ &\quad + \mathbf{v}_{\text{SINS}}^n \times (2\delta \boldsymbol{\omega}_{ie}^n + \delta \boldsymbol{\omega}_{en}^n) + \mathbf{C}_b^n \nabla_{ib}^b \\ \delta \dot{L} &= \delta v_N / (R_M + h) - v_N \delta h / (R_M + h^2) \\ \delta \dot{\lambda} &= \sec L \delta v_E / (R_N + h) + v_E \tan L \sec L \delta L / (R_N + h) \\ &\quad - v_E \sec L \delta h / (R_N + h)^2 \\ \delta \dot{h} &= \delta v_U \\ \dot{\boldsymbol{\epsilon}}_{ib}^b &= \mathbf{0}_{3 \times 1} \\ \dot{\nabla}_{ib}^b &= \mathbf{0}_{3 \times 1} \end{aligned} \quad (12)$$

where  $\delta \mathbf{v}_{\text{SINS}}^n$  denotes the velocity error of SINS.  $\delta \mathbf{p}_{\text{SINS}} = [\delta L \ \delta \lambda \ \delta h]^T$  denotes the position error vectors of SINS.  $L$ ,  $\lambda$ , and  $h$  are the local latitude, local longitude, and local altitude, respectively.  $\boldsymbol{\omega}_{in}^n$  is the angular rate of the  $n$  frame relative to the inertial frame in the  $n$  frame,  $\boldsymbol{\omega}_{en}^n$  denotes the angular rate of the  $n$  frame relative to the Earth frame in the  $n$  frame, and  $\boldsymbol{\omega}_{ie}^n$  is the Earth rotation rate in the  $n$  frame.  $\mathbf{f}^n$  denotes the specific force in the  $n$  frame.  $R_M$  and  $R_N$  are the principal radius of curvature of the prime meridian and the equator, respectively.  $\boldsymbol{\epsilon}_{ib}^b$  and  $\nabla_{ib}^b$  are the gyro constant bias and the accelerometer constant bias, respectively.  $\mathbf{v}_{\text{SINS}}^n = [v_E \ v_N \ v_U]^T$  and  $\mathbf{p}_{\text{SINS}} = [L \ \lambda \ h]^T$  are the velocity output and position output of SINS, respectively, and can be expressed as

$$\mathbf{v}_{\text{SINS}}^n = \mathbf{v}^n + \delta \mathbf{v}_{\text{SINS}}^n \quad (13)$$

$$\mathbf{p}_{\text{SINS}} = \mathbf{p} + \delta \mathbf{p}_{\text{SINS}} \quad (14)$$

where  $\mathbf{p}$  denotes the true position of the vehicle.

Due to the lever arm distance between GNSS and IMU, the  $n$  frames of GNSS and IMU are different, but they can be considered parallel to each other. By using the  $n$  frame of SINS as a reference, the velocity and position outputs of DGNSS can be written as follows:

$$\mathbf{v}_{\text{GNSS}} \approx \mathbf{v}^n + \mathbf{C}_b^n (\boldsymbol{\omega}_{eb}^b \times \mathbf{L}^b) \quad (15)$$

$$\mathbf{p}_{\text{GNSS}} \approx \mathbf{p} + \mathbf{F}_{pv} \mathbf{C}_b^n \mathbf{L}^b \quad (16)$$

$$\mathbf{F}_{pv} = \begin{bmatrix} 0 & \frac{1}{R_M + h} & 0 \\ \frac{\sec L}{R_M + h} & 0 & 0 \\ 0 & 0 & 1 \end{bmatrix} \quad (17)$$

where  $\mathbf{v}_{\text{GNSS}}$  and  $\mathbf{p}_{\text{GNSS}}$  are the velocity and position outputs of the DGNSS, respectively,  $\mathbf{L}^b$  is the lever arm from the IMU center to the phase center of the DGNSS antenna, and  $\boldsymbol{\omega}_{eb}^b$  is the angular rate of SINS relative to Earth in the  $b$  frame.

Based on (12), the error state vector of SINS/GNSS integrated navigation system is defined as

$$\mathbf{x}_k = [\boldsymbol{\varphi}^T \ \delta(\mathbf{v}_{\text{SINS}}^n)^T \ \delta \mathbf{p}_{\text{SINS}}^T \ (\boldsymbol{\epsilon}_{ib}^b)^T \ (\nabla_{ib}^b)^T]^T. \quad (18)$$

The system state equation is given by

$$\dot{\mathbf{x}}_k = \mathbf{F}_k \mathbf{x}_k + \mathbf{G}_k \mathbf{w}_k \quad (19)$$

where  $\mathbf{F}_k$  denotes the  $15 \times 15$  system state transition matrix and  $\mathbf{G}_k$  and  $\mathbf{w}_k$  are the noise transfer matrix and the system noise vector, respectively. These matrices can be determined from (12).

By using the difference in velocity and position between SINS and GNSS as the system measurement, the measurement equation can be written as

$$\mathbf{z}_k = \begin{bmatrix} \mathbf{v}_{\text{SINS}}^n + \mathbf{C}_b^n (\boldsymbol{\omega}_{eb}^b \times \mathbf{L}^b) - \mathbf{v}_{\text{GNSS}} \\ \mathbf{p}_{\text{SINS}} + \mathbf{F}_{pv} \mathbf{C}_b^n \mathbf{L}^b - \mathbf{p}_{\text{GNSS}} \end{bmatrix} = \mathbf{H}_k \mathbf{x}_k + \mathbf{v}_k \quad (20)$$

where  $\mathbf{H}_k = [\mathbf{0}_{6 \times 3} \ \mathbf{I}_6 \ \mathbf{0}_{6 \times 6}]$  denotes the measurement transition matrix and  $\mathbf{v}_k$  is the zero-mean Gaussian white noise vector.

One condition for the standard Kalman filter to be optimal in the sense of unbiased minimum variance is that both system and measurement noise follow a Gaussian distribution. However, if either type of noise is non-Gaussian, the performance of the filter is inevitably degraded, particularly when measurement errors are large. In practical application environments, especially in urban and forest environments, GNSS signals may frequently be occluded or interrupted. This will cause the assumptions of the standard Kalman filter to be violated, leading to reduced accuracy in SINS/GNSS integrated navigation. To reduce the impact of GNSS outliers on the results of SINS/GNSS integrated navigation, multiple fading factors are introduced to inflate the measurement noise covariance matrix to improve the robustness of the SINS/GNSS integrated navigation system.

The new measurement noise covariance matrix is defined as

$$\hat{\mathbf{R}}_k = \mathbf{S}_k \mathbf{R}_k \mathbf{S}_k^T \quad (21)$$

where  $\mathbf{S}_k = \text{diag}\{s_1 \ s_2 \ \dots \ s_n\}$ ,  $s_i$  is the fading factor corresponding to the  $i$ th measurement component  $\mathbf{z}_k^{(i)}$ , and  $n$  is the dimension of the measurement value.

The innovation vector of the filter is

$$\mathbf{e}_k = \mathbf{z}_k - \mathbf{H}_k \mathbf{x}_{k|k-1} \quad (22)$$

where  $\mathbf{x}_{k|k-1}$  denotes the one-step prediction of system state in the Kalman filter.

Under the Gaussian assumption, the distribution covariance of  $\mathbf{e}_k$  is

$$\mathbf{C}_k = \mathbf{H}_k \mathbf{P}_{k|k-1} \mathbf{H}_k^T + \mathbf{R}_k \quad (23)$$

where  $\mathbf{P}_{k|k-1}$  denotes the covariance matrix corresponding to  $\mathbf{x}_{k|k-1}$ .

The equally weighted recursive estimation method for  $\mathbf{C}_k$  can be constructed as

$$\begin{aligned} \hat{\mathbf{C}}_k &= \frac{1}{k} \sum_{i=1}^k (\mathbf{H}_i \mathbf{P}_{i|i-1} \mathbf{H}_i^T + \mathbf{R}_i) \\ &= \frac{1}{k} \left[ \sum_{i=1}^{k-1} (\mathbf{H}_i \mathbf{P}_{i|i-1} \mathbf{H}_i^T + \mathbf{R}_i) + (\mathbf{H}_k \mathbf{P}_{k|k-1} \mathbf{H}_k^T + \mathbf{R}_k) \right] \\ &= \left(1 - \frac{1}{k}\right) \hat{\mathbf{C}}_{k-1} + \frac{1}{k} (\mathbf{H}_k \mathbf{P}_{k|k-1} \mathbf{H}_k^T + \mathbf{R}_k) \\ &= \left(1 - \frac{1}{k}\right) \hat{\mathbf{C}}_{k-1} + \frac{1}{k} (\mathbf{e}_k \mathbf{e}_k^T). \end{aligned} \quad (24)$$

To improve the adaptive ability of (21), it is rewritten as

$$\hat{\mathbf{C}}_k = (1 - \eta_k) \mathbf{C}_{k-1} + \eta_k \mathbf{e}_k \mathbf{e}_k^T \quad (25)$$

where  $\eta_k = \eta_{k-1}/(\eta_{k-1} + b)$ ,  $\eta_0 = 1$ , and  $0 < b < 1$  is the decay factor and is typically set to  $b = 0.9 \sim 0.999$ .

To solve for  $S_k$ , we have the following expression:

$$\hat{\mathbf{C}}_k = \mathbf{H}_k \mathbf{P}_{k|k-1} \mathbf{H}_k^T + \hat{\mathbf{R}}_k = \mathbf{H}_k \mathbf{P}_{k|k-1} \mathbf{H}_k^T + S_k \mathbf{R}_k S_k^T. \quad (26)$$

It can be derived from (26) that

$$S_k(i) = \max \left( 1, \sqrt{\frac{N_k(i, i)}{\mathbf{R}_k(i, i)}} \right) \quad (27)$$

where

$$N_k = \hat{\mathbf{C}}_k - \mathbf{H}_k \mathbf{P}_{k|k-1} \mathbf{H}_k^T. \quad (28)$$

It is important to note that  $s_i$  should not be less than 1. This is because, in the presence of GNSS outliers, the measurement noise covariance matrix should be inflated to reduce the weight of the observations in the filtering process.

To avoid affecting the normal structure of the filter and increasing computational burden through excessive use of fading factors, the Mahalanobis distance of innovation vector is introduced to determine whether the fading factors are required. The Mahalanobis distance denotes the distance between two vectors and can be expressed as

$$M(\mathbf{a}, \mathbf{b}) = \sqrt{(\mathbf{a} - \mathbf{b})^T \Sigma^{-1} (\mathbf{a} - \mathbf{b})} \quad (29)$$

where  $\Sigma$  is the covariance matrix.

When the innovation vector follows a Gaussian distribution, its Mahalanobis distance should be chi-square distributed with degrees of freedom equal to the dimension of the innovation vector

$$f_k = \mathbf{e}_k^T [\mathbf{H}_k \mathbf{P}_{k|k-1} \mathbf{H}_k^T + \mathbf{R}_k]^{-1} \mathbf{e}_k \sim \chi^2(n). \quad (30)$$

Based on (30), the judgment criterion is

$$\begin{cases} f_k \leq T_D, & \text{The fading factor is not introduced} \\ f_k > T_D, & \text{The fading factor is introduced} \end{cases} \quad (31)$$

where  $T_D$  denotes the preset threshold and can be obtained by the freedom degree and required significance level of the chi-square distribution.

### 2) Calibration Process Based on Position Observation:

Based on the LDV error model described in Section II and considering the effect of the lever arm between the IMU and LDV (in the future, due to the limitations of the installation conditions, the LDV may not always be installed together with the IMU), the online calibration of the SINS/LDV integrated navigation system can be achieved by transforming the calibration parameters into a part of the state variables of the integrated navigation system. For the Kalman filter design of the calibration process based on position observation, the error state vector is defined as

$$\mathbf{x}_k^1 = [\delta\boldsymbol{\varphi}^T \quad \delta\mathbf{p}_{\text{DR}}^T \quad \delta\phi_{mx} \quad \delta\phi_{mz} \quad \delta K']^T \quad (32)$$

where  $\delta\boldsymbol{\varphi}$  denotes the residual attitude error of SINS after the SINS/GNSS integrated navigation process and  $\delta\mathbf{p}_{\text{DR}} = [\delta L_{\text{DR}} \quad \delta\lambda_{\text{DR}} \quad \delta h_{\text{DR}}]^T$  denotes the DR position error vectors of SINS/LDV integrated navigation system.  $\delta\phi_{mx}$  and  $\delta\phi_{mz}$  are the pitch installation misalignment angle and heading installation misalignment angle between the  $m$  frame and the  $b$  frame, respectively, after the coarse calibration process.  $\delta K'$  denotes the scale factor error after the coarse calibration process.

When considering the effect of the lever arm between IMU and LDV, the following relationship holds between the velocities in the  $b$  and  $m$  frames:

$$\mathbf{v}^b = \mathbf{C}_m^b \mathbf{v}^m - \boldsymbol{\omega}_{eb}^b \times \mathbf{L}_{\text{LDV}}^b \quad (33)$$

where  $\mathbf{L}_{\text{LDV}}^b$  is the level arm between the IMU and the LDV.

After completing the coarse calibration process, the velocity of the LDV in the  $n$  frame can be expressed as

$$\mathbf{v}_{\text{LDV}}^n = \tilde{\mathbf{C}}_b^n \tilde{\mathbf{C}}_m^b \tilde{K} \mathbf{v}_{\text{LDV}}^m - \tilde{\mathbf{C}}_b^n (\boldsymbol{\omega}_{eb}^b \times \mathbf{L}_{\text{LDV}}^b) \quad (34)$$

where the attitude matrix  $\tilde{\mathbf{C}}_b^n$  is provided by the SINS/GNSS integrated navigation system,  $\tilde{K}$  is the scale factor of LDV after the coarse calibration process, and the transformation matrix  $\tilde{\mathbf{C}}_m^b$ , following the  $y$ - $x$ - $z$  rotation sequence, can be calculated as in (35), shown at the bottom of the next page, where

$$\begin{aligned} \mathbf{C}_x(\tilde{\phi}_{mx}) &= \begin{bmatrix} 1 & 0 & 0 \\ 0 & \cos \tilde{\phi}_{mx} & -\sin \tilde{\phi}_{mx} \\ 0 & \sin \tilde{\phi}_{mx} & \cos \tilde{\phi}_{mx} \end{bmatrix} \\ \mathbf{C}_y(\tilde{\phi}_{my}) &= \begin{bmatrix} \cos \tilde{\phi}_{my} & 0 & \sin \tilde{\phi}_{my} \\ 0 & 1 & 0 \\ -\sin \tilde{\phi}_{my} & 0 & \cos \tilde{\phi}_{my} \end{bmatrix} \\ \mathbf{C}_z(\tilde{\phi}_{mz}) &= \begin{bmatrix} \cos \tilde{\phi}_{mz} & -\sin \tilde{\phi}_{mz} & 0 \\ \sin \tilde{\phi}_{mz} & \cos \tilde{\phi}_{mz} & 0 \\ 0 & 0 & 1 \end{bmatrix}. \end{aligned} \quad (35)$$

Since the roll installation misalignment angle has no effect on the SINS/LDV integrated navigation system,  $\tilde{\phi}_{my} = 0$ .

Since (34) is derived based on the NHC, errors may occur in the equation when the vehicle's motion state does not fully satisfy the NHC assumptions. This can ultimately affect the filtering results. Therefore, it is necessary to compensate for

the lateral velocity of the LDV in the  $m$  frame when the NHC is violated. Based on the results of the coarse calibration, the velocity projection of the SINS/GNSS integrated navigation system in the  $m$  frame can be expressed as

$$\tilde{\mathbf{v}}^m = [v_l \quad v_f \quad v_v] = \tilde{\mathbf{C}}_b^m \tilde{\mathbf{C}}_n^b \mathbf{v}^n. \quad (37)$$

To mitigate the effects of outliers, we express the lateral velocity of the vehicle used to compensate for the LDV lateral velocity in the  $m$  frame at moment  $k$  as

$$v_{\text{lateral}} = \frac{1}{N} \sum_{i=k-N+1}^k v_{l(i)} \quad (38)$$

where  $N$  is the preset value and  $v_{l(i)}$  denotes the value of  $v_l$  at moment  $i$ .

It is well known that a vehicle is prone to sideslip when turning, thus violating the NHC. In addition, according to vehicle dynamics, the forward velocity of the vehicle is a factor affecting its lateral acceleration [37]. Therefore, whether the NHC is violated can be determined based on the vehicle's traveling velocity and angular increment. Equation (3) can then be written as

$$\hat{\mathbf{v}}_{\text{LDV}}^m = \begin{cases} \left[ \begin{array}{ccc} 0 & \tilde{v}_{\text{LDV}} & 0 \end{array} \right]^T, & A_z \tilde{K} \tilde{v}_{\text{LDV}} \leq T_{\text{NHC}} \\ \left[ \begin{array}{ccc} v_{\text{lateral}} & \tilde{v}_{\text{LDV}} & 0 \end{array} \right]^T, & A_z \tilde{K} \tilde{v}_{\text{LDV}} > T_{\text{NHC}} \end{cases} \quad (39)$$

where  $T_{\text{NHC}}$  is the preset threshold and  $A_z$  denotes the angular increment of the  $z$ -gyro output.

According to (39), (34) can then be written as

$$\begin{aligned} \hat{\mathbf{v}}_{\text{LDV}}^n &= [\hat{\mathbf{v}}_{\text{LDV}(E)}^n \quad \hat{\mathbf{v}}_{\text{LDV}(N)}^n \quad \hat{\mathbf{v}}_{\text{LDV}(U)}^n]^T \\ &= \tilde{\mathbf{C}}_b^n \hat{\mathbf{v}}_{\text{LDV}}^b - \tilde{\mathbf{C}}_b^n (\omega_{eb}^b \times \mathbf{L}_{\text{LDV}}^b) \\ &= \tilde{\mathbf{C}}_b^n \tilde{\mathbf{C}}_m^b \tilde{\mathbf{K}} \hat{\mathbf{v}}_{\text{LDV}}^m - \tilde{\mathbf{C}}_b^n (\omega_{eb}^b \times \mathbf{L}_{\text{LDV}}^b) \\ &\approx (\mathbf{I}_3 - (\delta\phi) \times) \mathbf{C}_b^n (\mathbf{I}_3 - (\delta\phi_m) \times) \mathbf{C}_m^b (1 + \delta K) \tilde{\mathbf{K}} \mathbf{v}^m \\ &\quad - (\mathbf{I}_3 - (\delta\phi) \times) \mathbf{C}_b^n (\omega_{eb}^b \times \mathbf{L}_{\text{LDV}}^b) \\ &\approx (\mathbf{I}_3 - (\delta\phi) \times) \mathbf{C}_b^n (\mathbf{I}_3 - (\delta\phi_m) \times) \mathbf{C}_m^b (1 + \delta K') \mathbf{v}^m \\ &\quad - (\mathbf{I}_3 - (\delta\phi) \times) \mathbf{C}_b^n (\omega_{eb}^b \times \mathbf{L}_{\text{LDV}}^b) \end{aligned} \quad (40)$$

where  $\delta\phi_m = [\delta\phi_{mx} \quad 0 \quad \delta\phi_{mz}]^T$  denotes the residual of the installation misalignment angle vector.

Given an initial position and using the velocity data obtained from (40), DR can be performed. Assuming that other influencing factors are negligible, the error  $\delta\mathbf{p}_{\text{DR}}$  between the DR-determined position  $\mathbf{p}_{\text{DR}}$  and the actual position  $\mathbf{p}$  can be considered to be caused by the error in (40). In other words, the three error parameters of the LDV ultimately propagate to the position error of the integrated navigation system.

Similar to the rate of change of position error for the SINS/GNSS integrated navigation system described in (12), the rate of change of position error for the DR system is depicted as follows:

$$\delta\dot{\mathbf{p}}_{\text{DR}} = \mathbf{F}_{pp}\delta\mathbf{p}_{\text{DR}} + \mathbf{F}_{pv}\delta\hat{\mathbf{v}}_{\text{LDV}}^n \quad (41)$$

where

$$\mathbf{F}_{pp} = \begin{bmatrix} 0 & 0 & \frac{-\hat{\mathbf{v}}_{\text{LDV}(N)}^n}{(R_M + h_{\text{DR}})^2} \\ \frac{\hat{\mathbf{v}}_{\text{LDV}(E)}^n \tan L_{\text{DR}} \sec L_{\text{DR}}}{R_N + h_{\text{DR}}} & 0 & \frac{-\hat{\mathbf{v}}_{\text{LDV}(E)}^n \sec L_{\text{DR}}}{(R_N + h_{\text{DR}})^2} \\ 0 & 0 & 0 \end{bmatrix} \quad (42)$$

$$\mathbf{F}_{pv} = \begin{bmatrix} 0 & \frac{1}{R_M + h_{\text{DR}}} & 0 \\ \frac{\sec L_{\text{DR}}}{R_M + h_{\text{DR}}} & 0 & 0 \\ 0 & 0 & 1 \end{bmatrix} \quad (43)$$

$$\delta\hat{\mathbf{v}}_{\text{LDV}}^n \approx (\mathbf{v}^n \times) \delta\phi + \mathbf{C}_b^n (\mathbf{v}^b \times) \delta\phi_m + \delta K' \mathbf{v}^n \quad (44)$$

where

$$\mathbf{v}^n = \mathbf{C}_b^n \mathbf{v}^b = \mathbf{C}_b^n (\mathbf{C}_m^b \mathbf{v}^m - \omega_{eb}^b \times \mathbf{L}_{\text{LDV}}^b) \quad (45)$$

where  $\mathbf{v}^b$  denotes the vehicle true velocity in the  $b$  frame.

Since the vehicle attitude obtained by the SINS/GNSS integrated navigation system is sufficiently accurate, the residual attitude error of SINS can be considered a random constant. Its error model is  $\delta\phi = \mathbf{0}_{3 \times 1}$ .

Given the exceptional performance of the LDV and the fixed installation relationship between the LDV and the SINS, both the scale factor error and installation misalignment angle error of LDV are modeled as random constants. As such, the following error equations are obtained:

$$\begin{aligned} \delta\dot{K}' &= 0 \\ \delta\dot{\phi}_{mx} &= 0 \\ \delta\dot{\phi}_{mz} &= 0. \end{aligned} \quad (46)$$

Summing up, based on (32), (41), (44), and (46), the state equation of the SINS/LDV online calibration filter system is given by

$$\dot{\mathbf{x}}_k^1 = \mathbf{F}_k^1 \mathbf{x}_k^1 + \mathbf{G}_k^1 \mathbf{w}_k^1 \quad (47)$$

where  $\mathbf{F}_k^1$  is the  $9 \times 9$  system state transition matrix,  $\mathbf{G}_k^1$  is the noise transfer matrix, and  $\mathbf{w}_k^1$  is the system noise vector. These matrices can be determined from (41), (44), and (46).

By using the position difference between the SINS/LDV DR system and the SINS/GNSS integrated navigation system

$$\begin{aligned} \tilde{\mathbf{C}}_m^b &= \mathbf{C}_z(\tilde{\phi}_{mz}) \mathbf{C}_x(\tilde{\phi}_{mx}) \mathbf{C}_y(\tilde{\phi}_{my}) \\ &= \begin{bmatrix} \cos \tilde{\phi}_{my} \cos \tilde{\phi}_{mz} - \sin \tilde{\phi}_{mx} \sin \tilde{\phi}_{my} \sin \tilde{\phi}_{mz} & -\cos \tilde{\phi}_{mx} \sin \tilde{\phi}_{mz} & \sin \tilde{\phi}_{my} \cos \tilde{\phi}_{mz} + \sin \tilde{\phi}_{mx} \cos \tilde{\phi}_{my} \sin \tilde{\phi}_{mz} \\ \cos \tilde{\phi}_{my} \sin \tilde{\phi}_{mz} + \sin \tilde{\phi}_{mx} \sin \tilde{\phi}_{my} \cos \tilde{\phi}_{mz} & \cos \tilde{\phi}_{mx} \cos \tilde{\phi}_{mz} & \sin \tilde{\phi}_{my} \sin \tilde{\phi}_{mz} - \sin \tilde{\phi}_{mx} \cos \tilde{\phi}_{my} \cos \tilde{\phi}_{mz} \\ -\cos \tilde{\phi}_{mx} \sin \tilde{\phi}_{my} & \sin \tilde{\phi}_{mx} & \cos \tilde{\phi}_{my} \cos \tilde{\phi}_{mz} \end{bmatrix} \end{aligned} \quad (35)$$

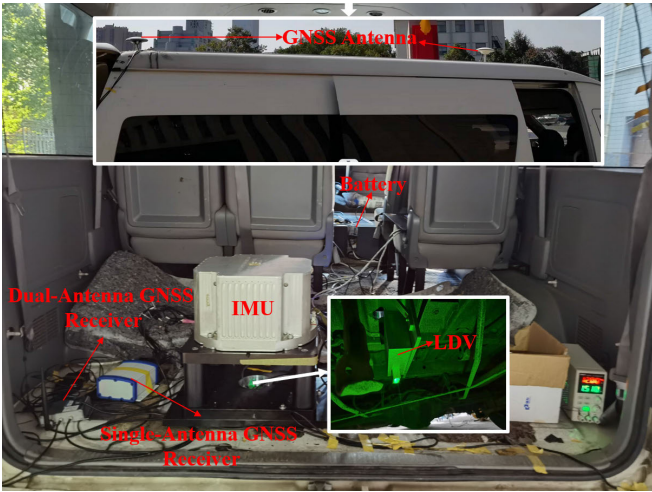


Fig. 5. Installation diagram of the experimental system.

as the system measurement, the measurement equation can be written as

$$\mathbf{z}_k^1 = [\mathbf{p}_{\text{DR}} - \mathbf{p}] = \mathbf{H}_k^1 \mathbf{x}_k^1 + \mathbf{v}_k^1 \quad (48)$$

where  $\mathbf{H}_k^1 = [\mathbf{0}_{3 \times 3} \ I_3 \ \mathbf{0}_{3 \times 3}]$  denotes the measurement transition matrix and  $\mathbf{v}_k^1$  is the measurement noise (zero-mean Gaussian white noise).

#### IV. VEHICLE-MOUNTED FIELD TEST

To evaluate the effectiveness of the calibration method proposed in this article and its practical value, two groups of vehicle-mounted tests were conducted. As shown in Fig. 5, the test equipment includes a self-developed high-precision IMU, a self-made 1D-LDV, a dual-antenna DGNSS receiver, and a single-antenna DGNSS receiver as a backup. The high-precision IMU consists of three-ring laser gyros and three quartz accelerometers with an output frequency of 100 Hz. The bias instability of the gyros is within 0.007°/h and their random walk is within 0.001°/√h. The bias instability of the accelerometers is within 50 μg and their random walk is 50 μg/√h. The velocity measurement error of the LDV is within 0.08% ( $1\sigma$ ) with an output frequency of 100 Hz. The dual-antenna DGNSS receiver integrates microelectromechanical system (MEMS) inertial sensors. The horizontal positioning accuracy, altitude positioning accuracy, and velocity accuracy of this DGNSS receiver are within 0.05 m, 0.05 m, and 0.03 m/s, respectively, with an output frequency of 10 Hz. The spare single-antenna DGNSS receiver does not integrate any other inertial sensors. The horizontal positioning accuracy, altitude positioning accuracy, and velocity accuracy of this DGNSS receiver are within 0.1 m, 0.1 m, and 0.03 m/s, respectively, with an output frequency of 5 Hz.

Two groups of field tests were conducted in Changsha City. At the starting point, the vehicle remained stationary for approximately 13 min before moving. During this period, a static attitude alignment was performed to obtain an accurate initial attitude. The reference position of the vehicle was obtained by the high-precision SINS/GNSS integrated navigation system, which combines a high-precision IMU and

a dual-antenna DGNSS and applies the Rauch–Tung–Striebel (RTS) smoothing algorithm to process the data. In this article, the outputs of dual-antenna DGNSS are used to validate the accuracy of our proposed calibration method because the dual-antenna DGNSS used in the experiments integrates MEMS sensors, which can provide high positioning accuracy even in the case of short-term GNSS signal loss. Also, the outputs of single-antenna DGNSS are used to validate the robustness of our proposed calibration method because the single-antenna DGNSS used in the experiments does not integrate with any other inertial sensors, which cannot locate the position in the absence of GNSS signals.

To evaluate the calibration performance of the proposed method, the following three methods are designed for comparison.

*Method 1:* The calibration method is proposed in this article.

*Method 2:* The position observation-based SINS/LDV calibration method was proposed in [34]. In this method, the attitude information of the SINS/GNSS integrated navigation system, the GNSS position output, and the LDV output are used to establish position observations. The scale factor error of the LDV is determined by the ratio of two observation vector moduli, and the misalignment angle of the LDV is determined by solving for two observation vectors using Davenport's q-method.

*Method 3:* The velocity observation-based SINS/LDV calibration method was proposed in [30]. The method adds an analytic coarse calibration process, to obtain coarse estimates of the LDV scale factor and the heading installation misalignment angle, before performing a traditional Kalman filter-based calibration.

*Method 4:* Based on Method 1, the lateral velocity of the LDV is no longer compensated.

The first vehicle test lasted 2.27 h and covered a total distance of 76.9 km. Fig. 6 shows the vehicle trajectory and the LDV output. Figs. 7–9 show the calibration results of different methods in the first test. As shown in Figs. 7–9, all four calibration models can estimate the calibration parameters of the SINS/LDV integrated navigation system. Methods 1, 3, and 4 have a faster error convergence speed than Method 2, indicating that performing a coarse calibration prior to the start of the calibration process can accelerate error convergence and improve the calibration speed. As can be seen from Figs. 8 and 9, the calibration curve corresponding to Method 3 has frequent and large fluctuations around 0.1–0.2 h, which is because during this period, the vehicles often passed through urban canyons and overpasses, resulting in frequent interference of GNSS signals. This is also the reason for the slow convergence of Method 2. Because the position observation vector used in Method 2 is based on the accumulation of GNSS position increment and LDV output velocity, the outliers of GNSS and LDV will undoubtedly have a large and lasting impact on the accuracy of the position observation vector in the early stage of the calibration process when the accumulation value is not large enough. Compared with Method 3, which also carried out a rough calibration process, the calibration curves of Methods 1 and 4 are more stable for two reasons. First, Methods 1 and 4 use the SINS/GNSS

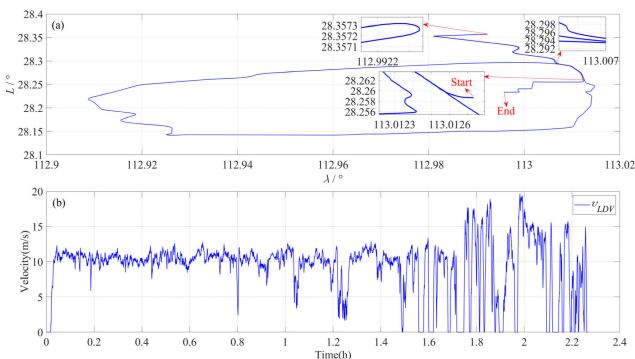


Fig. 6. (a) Trajectory of the vehicle in the first field test. (b) Velocity curve of LDV output in the first field test.

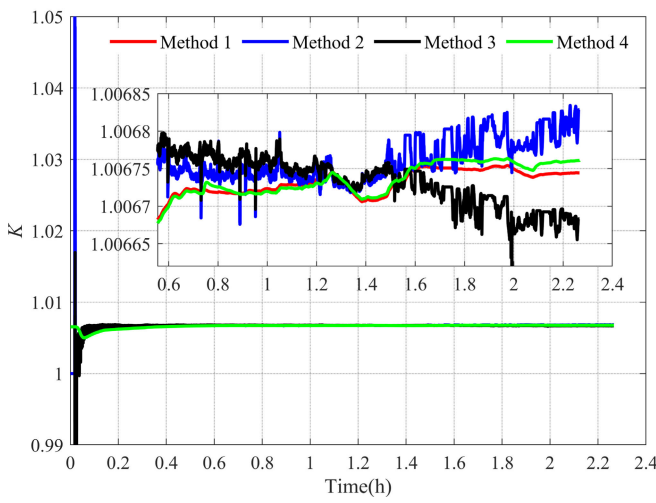


Fig. 7. Curve of the scale factor in the first vehicle test.

integrated navigation system information, instead of directly using the GNSS output. This reduces the influence of GNSS outliers and noise on the calibration process to a great extent. Second, Methods 1 and 4 use position observations rather than velocity observations. Compared with velocity, the position trajectory has a much larger magnitude than the corresponding outliers and noise. The subplots in Figs. 7 and 8 show that the estimation curve of Method 1 is more stable than that of Method 4, suggesting that compensating for the lateral velocity of the LDV in the  $m$  frame in particular scenarios is effective. In addition, Figs. 8 and 9 show that the estimation curves of Methods 1, 3, and 4 experience different degrees of fluctuation around 2600 s, with Method 3 having the largest magnitude of fluctuation and Method 1 having the smallest. To identify the cause of the fluctuation, we plot the pitch installation misalignment angle, the angular velocity of heading, the lateral velocity of GNSS in the  $m$  frame [ $v_{GNSS}^m(1)$ ], and the output of LDV in the range of 2400–2900 s in Fig. 10.

Fig. 10(b) shows that the heading angular velocity exhibited a large fluctuation lasting for several tens of seconds during 2600–2700 s. In addition, the velocity curve of the LDV in Fig. 10(d) indicates that the vehicle did not decelerate significantly during that time period. Therefore, it can be inferred that the vehicle experienced a turning process with a

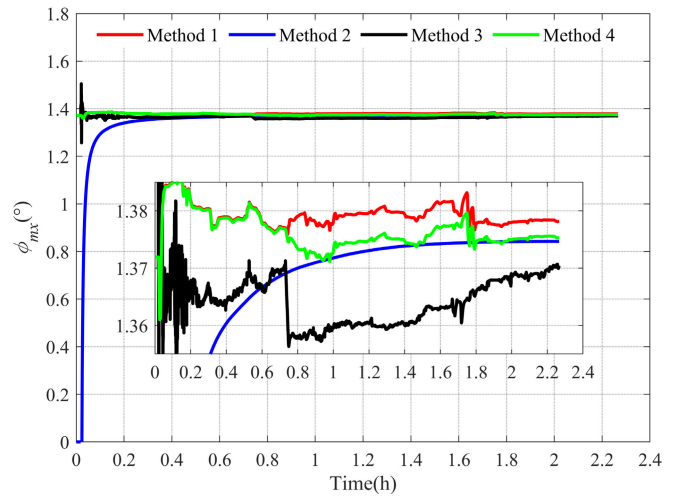


Fig. 8. Curve of the pitch misalignment angle in the first vehicle test.

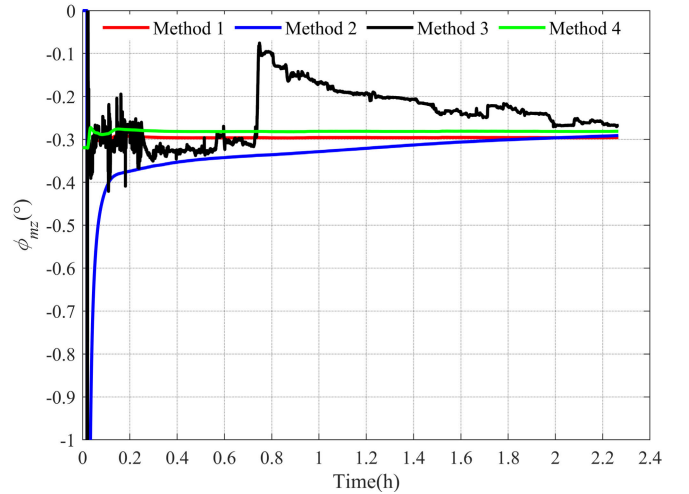


Fig. 9. Curve of the heading misalignment angle in the first vehicle test.

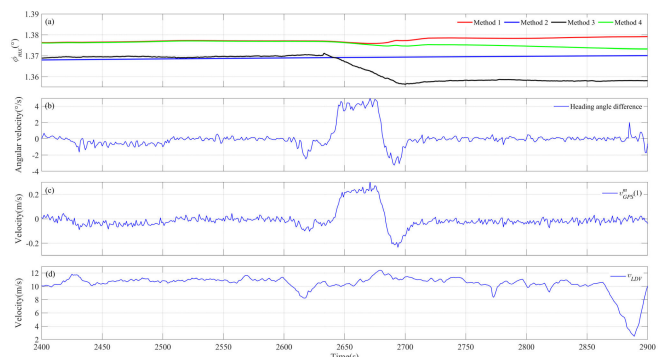


Fig. 10. (a) Curve of the pitch misalignment angle in 2400–2900 s of the first test. (b) Curve of the angular velocity of heading in 2400–2900 s of the first test. (c) Curve of  $v_{GNSS}^m(1)$  in 2400–2900 s of the first test. (d) Curve of the LDV output in 2400–2900 s of the first test.

faster vehicle velocity during 2600–2700 s. The variation trend of GNSS lateral velocity in the  $m$  frame during 2600–2700 s in Fig. 10(c) matches the variation trend of the heading angle velocity in Fig. 10(b), suggesting that the NHC lateral velocity is influenced by the change of vehicle heading angle. In other

**TABLE I**  
PERFORMANCE COMPARISON OF THE FOUR METHODS  
IN THE FIRST TEST (76.9 km)

Methods	Mean (m)	Error ratio (%)	Max (m)	Error ratio (%)
<i>Method 1</i>	<b>2.56</b>	<b>0.033</b>	<b>6.61</b>	<b>0.086</b>
	Height error	1.85	0.024	5.83
<i>Method 2</i>	Horizontal error	2.93	0.038	8.28
	Height error	4.97	0.065	9.06
<i>Method 3</i>	Horizontal error	5.22	0.068	9.94
	Height error	7.11	0.092	11.77
<i>Method 4</i>	Horizontal error	3.69	0.048	7.14
	Height error	3.74	0.049	7.68

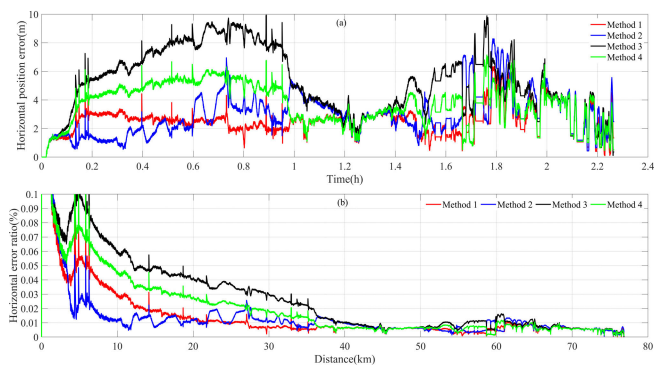


Fig. 11. (a) First test's horizontal location error. (b) First test's horizontal error ratio.

words, vehicle turns, especially high-speed turns, cause larger NHC lateral velocity and thus violate the NHC assumption. The trend of pitch misalignment angle in Fig. 10(a) is in line with this phenomenon. When the vehicle turns for a long time and causes the NHC to be violated for a long time, Method 3 based on velocity observation is most affected, while Methods 1, 2, and 4 based on position observation are less affected. Moreover, Method 1 with lateral velocity compensation is less affected than Method 4 without lateral velocity compensation. In conclusion, it is necessary to compensate for the lateral velocity of the LDV in the *m* frame when the NHC assumption is violated.

To evaluate the accuracy of the calibration results from all four methods, the DR of the SINS/LDV integrated navigation system is performed using the calibration results. The horizontal positioning error and ratio with respect to the distance traveled of different methods in the first test are compared in Fig. 11. The height positioning error of different methods in the first test is shown in Fig. 12. The maximum (Max) and mean (Mean) position errors of the SINS/LDV integrated navigation system calibrated by four different methods in the first test are summarized in Table I.

As shown in Figs. 11 and 12 and Table I, the positioning accuracy of the SINS/LDV integrated navigation system varies depending on the calibration method used. Method 1 yields the highest accuracy, while Method 3 yields the lowest accuracy. This suggests that Method 1 has the best calibration performance and Method 3 has the worst calibration performance.

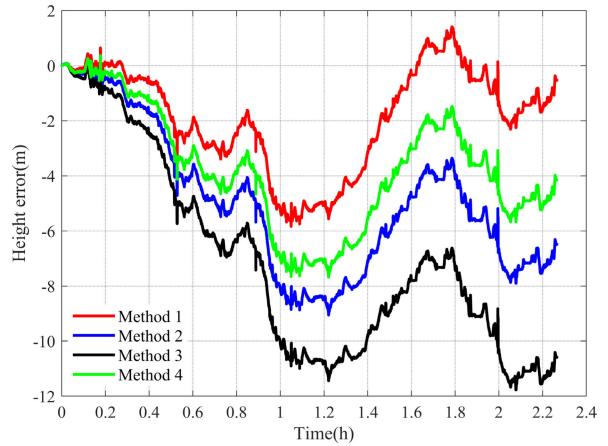


Fig. 12. First test's height positioning error.

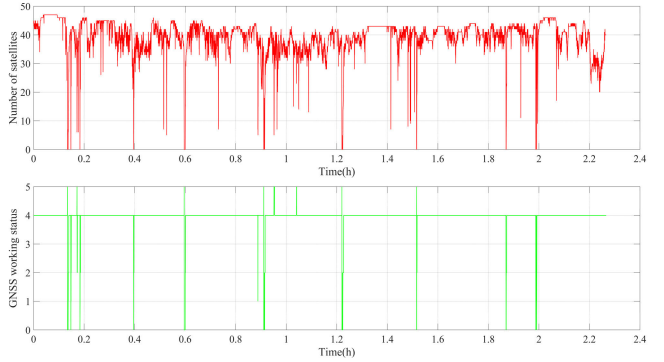


Fig. 13. Number of satellites and the GNSS working status during the first vehicle test.

in the first test, which is consistent with their respective performances in Figs. 7–9. However, in practice, not all GNSS receivers have internal integration of IMU or other inertial sensors, and most of them do not output position information when the signal is lost. In order to further test the robustness of the proposed method and its performance in the face of low-end and mid-range GNSS receivers, we calibrate the LDVs using the output of a spare GNSS in the experiments, namely, a single-antenna DGNSS without any other integrated inertial devices. Fig. 13 shows the number of satellites and the working status of the single-antenna DGNSS output during the first vehicle test. The operating states of the DGNSS are given as follows: State 4 indicates that GNSS outputs a fixed solution with the highest accuracy, generally within 0.1 m; State 5 indicates that GNSS outputs a floating-point solution with higher accuracy, generally within 3 m; States 2 and 1 indicate that GNSS outputs a differential solution and a single point solution, respectively, with lower accuracy, generally greater than 5 m; and State 0 indicates that GNSS fails, with no satellite data received. As shown in Fig. 13, the GNSS signals suffered from frequent failures and interference during the first test. The calibration results of Methods 1 and 2 using the data of the single-antenna DGNSS are shown in Fig. 14. The DR results of the SINS/LDV integrated navigation system

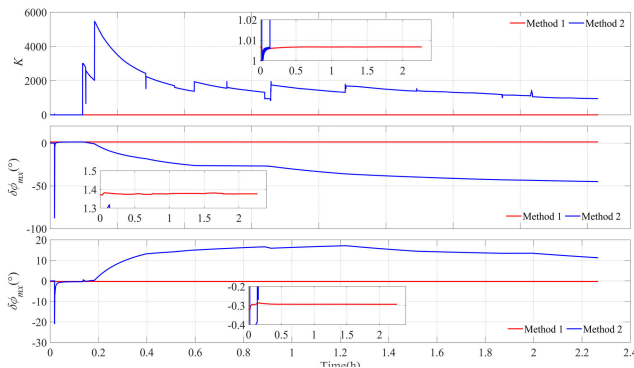


Fig. 14. Calibration results of Methods 1 and 2 under the actual GNSS data in the first test.

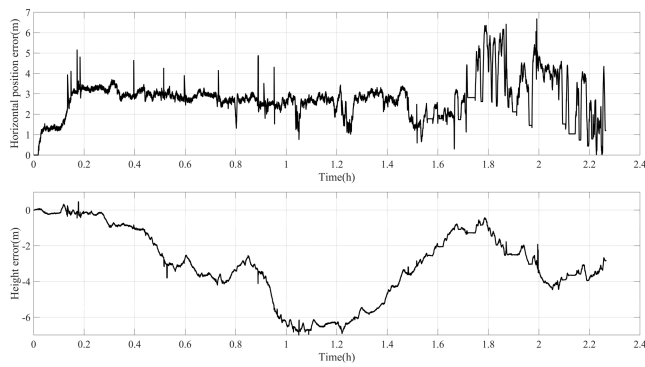


Fig. 15. First test's position error based on Fig. 14's calibration results of Method 1.

obtained using the calibration results of Method 1 in Fig. 14 are presented in Fig. 15.

As shown in Fig. 14, the calibration results of Method 2 diverge rapidly when the GNSS signal is interrupted, while the calibration results of Method 1 are almost unaffected. This is because the observation vector model in Method 2 directly uses the GNSS position information and relies on the accumulation of position increments throughout the calibration process. Therefore, Method 2 cannot effectively resist large GNSS outliers, and their effect will continue to affect the entire calibration process. Compared with Method 2, Method 1 proposed in this article introduces the adaptive multiple fading factors in the SINS/GNSS integrated navigation phase and flexibly adjusts the noise covariance matrix of the filter based on the Mahalanobis distance of the innovation vector, thus reducing the impact of GNSS outliers on the SINS/GNSS integrated navigation results. Moreover, the filter used to calibrate the SINS/LDV integrated navigation system is constructed based on the results of SINS/GNSS integrated navigation and the position information of SINS/LDV DR, rather than the output of GNSS. Therefore, Method 1 is a more suitable calibration method than Method 2 when the GNSS signal is not ideal. As shown in Fig. 15, the position errors of Method 1 are not significantly different from those in Figs. 11 and 12, again demonstrating the ability of Method 1 to resist GNSS outliers. To further verify the effectiveness and evaluate the accuracy of the proposed calibration method,

TABLE II  
PERFORMANCE COMPARISON OF THE FOUR METHODS IN THE SECOND TEST (65.34 km)

Methods		Mean (m)	Error ratio (%)	Max (m)	Error ratio (%)
<i>Method 1</i>	Horizontal error	<b>5.85</b>	<b>0.089</b>	<b>10.91</b>	<b>0.167</b>
	Height error	<b>0.02</b>	<b>0.001</b>	<b>2.71</b>	<b>0.041</b>
<i>Method 2</i>	Horizontal error	8.09	0.124	17.16	0.263
	Height error	3.55	0.054	5.98	0.092
<i>Method 3</i>	Horizontal error	5.18	0.079	11.93	0.183
	Height error	0.74	0.011	3.99	0.061
<i>Method 4</i>	Horizontal error	6.01	0.092	11.06	0.169
	Height error	2.67	0.041	7.18	0.110

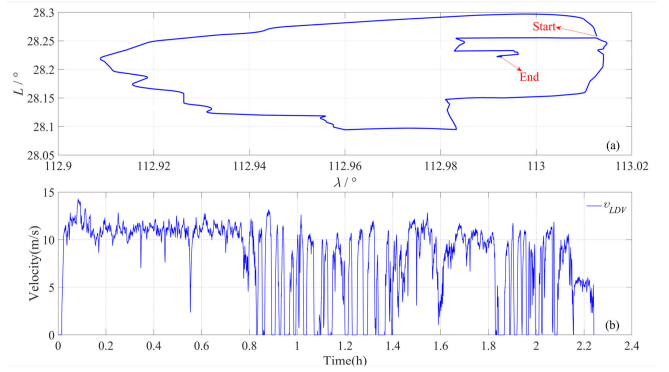


Fig. 16. (a) Trajectory of the vehicle in the second field test. (b) Velocity curve of LDV output in the second field test.

a second vehicle test was conducted that lasted 2.24 h and covered a total distance of 65.34 km. Test 2 used the same equipment and installation relationship as Test 1. The vehicle trajectory and the LDV output are shown in Fig. 16. The calibration results using the reference position information are presented in Figs. 17–19. The DR results of the SINS/LDV integrated navigation system calibrated by different methods are compared in Figs. 20 and 21 and Table II. The number of satellites and the GNSS working status of the single-antenna DGNSS output during the second vehicle test are shown in Fig. 22. The calibration results of Methods 1 and 2 using the data of the single-antenna DGNSS are shown in Fig. 23. The DR results of the SINS/LDV integrated navigation system obtained using the calibration results of Method 1 in Fig. 23 are presented in Fig. 24.

The results in Figs. 17–21 and Table II once again verify the superiority of the proposed Method 1. Method 1 exhibits the highest calibration accuracy and the fastest convergence speed among the four methods. The calibration curves of Methods 1, 2, and 4 based on position observation are smoother than those of Method 3 based on velocity observation. In addition, the results in Figs. 23 and 24 once again verify the robustness of Method 1, which can still accurately calibrate the SINS/LDV integrated navigation system when GNSS signals are frequently disturbed.

The calibration results of the two groups of tests are shown in Table III. When the installation relationship between IMU and LDV remains unchanged, the calibration results obtained

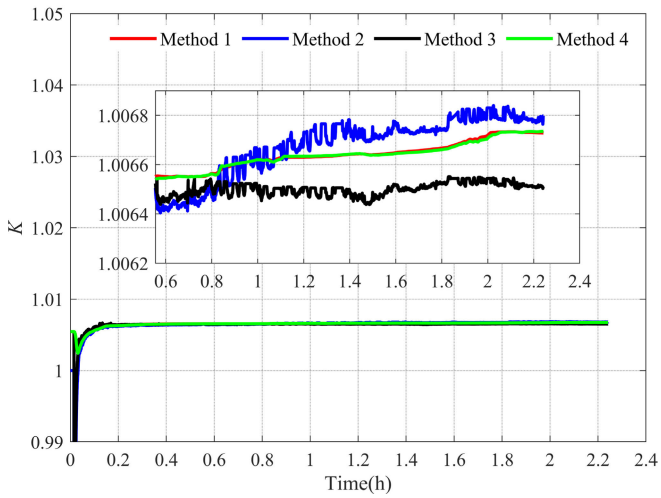


Fig. 17. Curve of the scale factor in the second vehicle test.

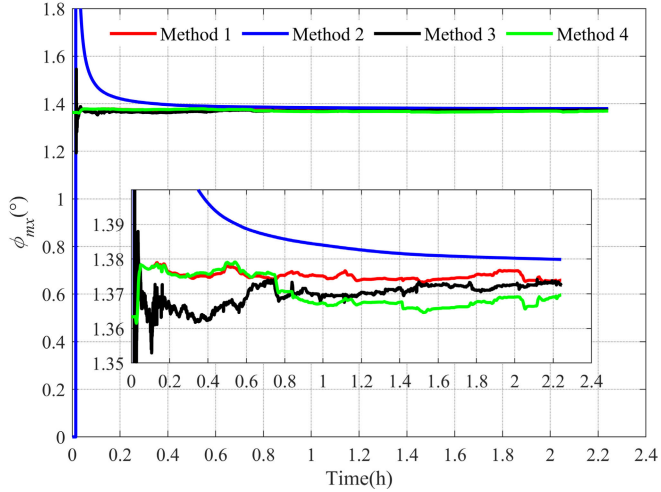


Fig. 18. Curve of the pitch misalignment angle in the second vehicle test.

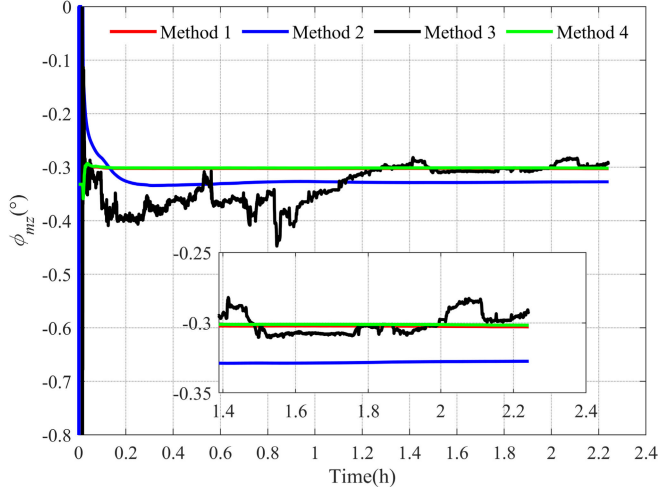


Fig. 19. Curve of the heading misalignment angle in the first vehicle test.

by the four calibration methods in the two groups of tests are similar, especially for the method proposed in this article, which has the closest calibration parameters in the two groups

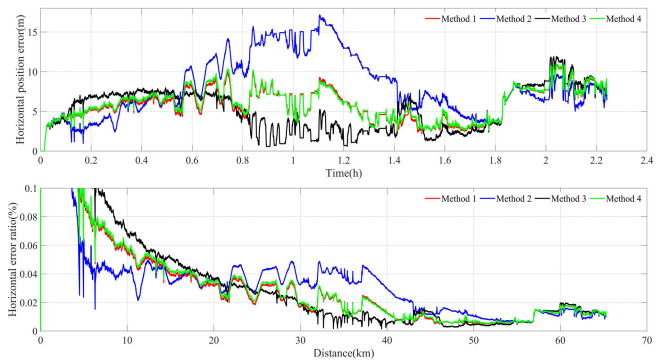


Fig. 20. Second test's horizontal location error and horizontal error ratio.

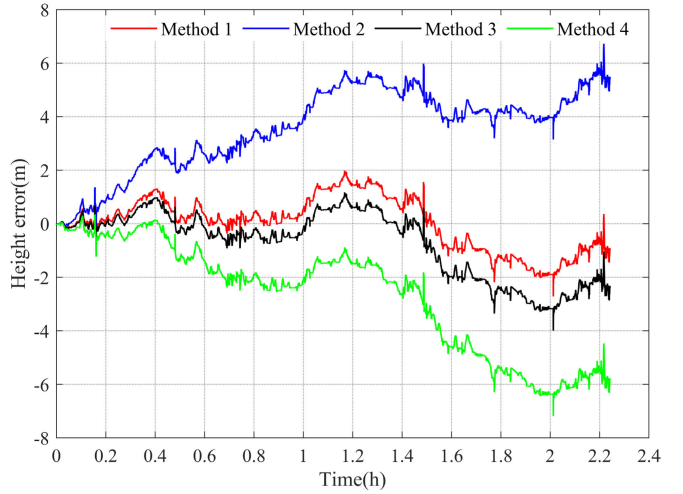


Fig. 21. Second test's height positioning error.

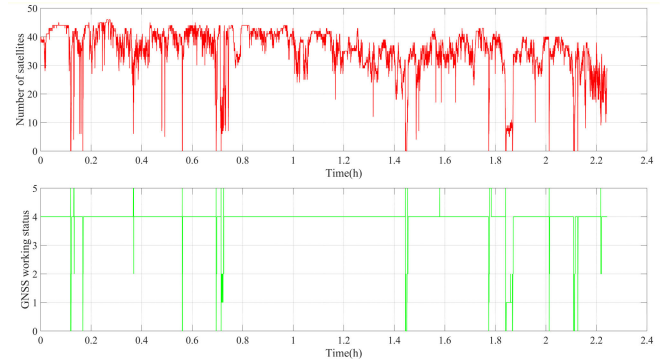


Fig. 22. Number of satellites and the GNSS working status during the second vehicle test.

of tests. To verify the generalizability and accuracy of the calibration method proposed in this article, the calibration results of the two groups of tests were cross-verified; that is, the calibration results of the first group and the second group were substituted into the data of the second group and the first group, respectively, for the DR, and the position errors obtained are shown in Figs. 25 and 26.

By comparing Figs. 11 and 12 and Figs. 20 and 21 with Figs. 25 and 26, it can be seen that Method 1 proposed in this article still has the highest horizontal localization accuracy as

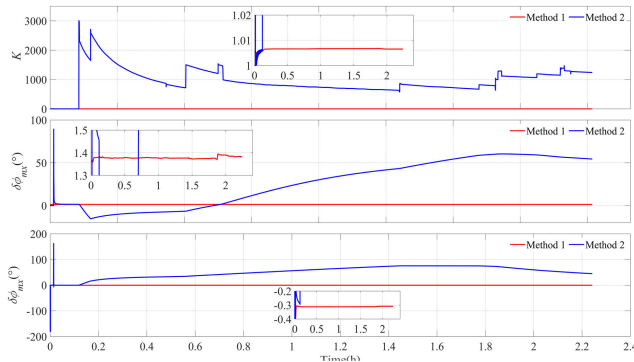


Fig. 23. Calibration results of Methods 1 and 2 under the actual GNSS data in the second test.

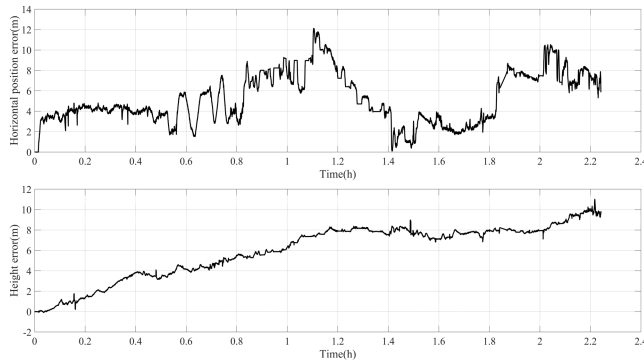


Fig. 24. Second test's position error based on Fig. 23's calibration results of Method 1.

TABLE III

CALIBRATION RESULTS OF THE FOUR METHODS IN TWO TESTS

Methods		$K$	$\phi_{mx}$ (deg)	$\phi_{mz}$ (deg)
<i>Method 1</i>	Test 1	1.00674	1.3782	-0.2957
	Test 2	1.00673	1.3740	-0.3029
<i>Method 2</i>	Test 1	1.00683	1.3746	-0.2911
	Test 2	1.00680	1.3799	-0.3273
<i>Method 3</i>	Test 1	1.00668	1.3704	-0.2675
	Test 2	1.00652	1.3725	-0.2921
<i>Method 4</i>	Test 1	1.00676	1.3753	-0.2812
	Test 2	1.00674	1.3697	-0.3017

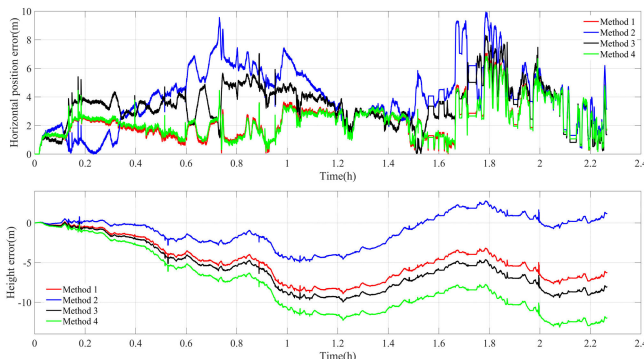


Fig. 25. Position error after substituting the test calibration results of the second group into the data of the first group.

well as satisfactory altitude accuracy in the cross validation of the two groups of tests, which indicates that the calibration method proposed in this article is effective and has universal applicability.

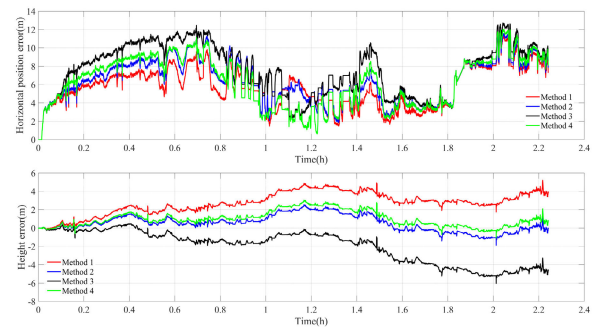


Fig. 26. Position error after substituting the test calibration results of the first group into the data of the second group.

## V. CONCLUSION

This article proposes a calibration method for the SINS/LDV integrated navigation system based on position observation. Compared with the existing main calibration methods for SINS/LDV integrated navigation system, the proposed method achieves higher calibration accuracy and robustness. Two groups of vehicle field tests were carried out to evaluate the performance of the proposed calibration method and three different calibration methods were used for comparison. The results show that the calibration method proposed in this article has the highest calibration accuracy among the four calibration methods. The total distances of the two groups of tests were 76.9 and 65.34 km. The maximum DR horizontal errors of the SINS/LDV integrated navigation system calibrated by the proposed method were 6.61 and 10.91 m, respectively, and the maximum DR height errors were less than 6 m in both tests. In addition, the robustness of the proposed calibration method was verified by using GNSS actual outputs in the two groups of tests.

## REFERENCES

- [1] D. H. Titterton, J. L. Weston, and J. L. Weston, *Strapdown Inertial Navigation Technology*. London, U.K.: Peter Peregrinus Limited, 1997.
- [2] P. D. Groves, *Principles of GNSS, Inertial, and Multisensor Integrated Navigation Systems*. Norwood, MA, USA: Artech House, 2008.
- [3] Z. Wen, G. Yang, Q. Cai, and T. Chen, "A novel Bluetooth-odometer-aided smartphone-based vehicular navigation in satellite-denied environments," *IEEE Trans. Ind. Electron.*, vol. 70, no. 3, pp. 3136–3146, Mar. 2023, doi: 10.1109/TIE.2022.3169714.
- [4] Z. Wen, G. Yang, and Q. Cai, "An improved SINS/NHC integrated navigation algorithm based on Ackermann turning geometry," *Measurement*, vol. 192, Mar. 2022, Art. no. 110859, doi: 10.1016/j.measurement.2022.110859.
- [5] H. Zhao, L. Miao, and H. Shao, "Adaptive two-stage Kalman filter for SINS/odometer integrated navigation systems," *J. Navigat.*, vol. 70, no. 2, pp. 242–261, Mar. 2017, doi: 10.1017/s0373463316000485.
- [6] Y. Huang, Y. Zhang, and X. Wang, "Kalman-filtering-based in-motion coarse alignment for odometer-aided SINS," *IEEE Trans. Instrum. Meas.*, vol. 66, no. 12, pp. 3364–3377, Dec. 2017, doi: 10.1109/TIM.2017.2737840.
- [7] M. Wang, W. Wu, X. He, Y. Li, and X. Pan, "Consistent ST-EKF for long distance land vehicle navigation based on SINS/OD integration," *IEEE Trans. Veh. Technol.*, vol. 68, no. 11, pp. 10525–10534, Nov. 2019, doi: 10.1109/TVT.2019.2939679.
- [8] W. Ouyang, Y. Wu, and H. Chen, "INS/odometer land navigation by accurate measurement modeling and multiple-model adaptive estimation," *IEEE Trans. Aerosp. Electron. Syst.*, vol. 57, no. 1, pp. 245–262, Feb. 2021, doi: 10.1109/TAES.2020.3011998.
- [9] J. Dong, X. Ren, S. Han, and S. Luo, "UAV vision aided INS/odometer integration for land vehicle autonomous navigation," *IEEE Trans. Veh. Technol.*, vol. 71, no. 5, pp. 4825–4840, May 2022, doi: 10.1109/TVT.2022.3151729.

- [10] H. Hu, K. Li, W. Liang, Q. Li, and Z. Xie, "Kilometer sign positioning-aided INS/odometer integration for land vehicle autonomous navigation," *IEEE Sensors J.*, vol. 23, no. 4, pp. 4143–4158, Feb. 2023, doi: [10.1109/JSEN.2023.3236063](https://doi.org/10.1109/JSEN.2023.3236063).
- [11] Z. Jian and L. Xingwu, "Research on laser Doppler velocimeter for vehicle self-contained inertial navigation system," *Opt. Laser Technol.*, vol. 42, no. 3, pp. 477–483, Apr. 2010, doi: [10.1016/j.optlastec.2009.09.001](https://doi.org/10.1016/j.optlastec.2009.09.001).
- [12] X. Nie and J. Zhou, "Pitch independent vehicle-based laser Doppler velocimeter," *Opt. Lasers Eng.*, vol. 131, Aug. 2020, Art. no. 106072, doi: [10.1016/j.optlaseng.2020.106072](https://doi.org/10.1016/j.optlaseng.2020.106072).
- [13] J. Zhou, X. Nie, and J. Lin, "A novel laser Doppler velocimeter and its integrated navigation system with strapdown inertial navigation," *Opt. Laser Technol.*, vol. 64, pp. 319–323, Dec. 2014, doi: [10.1016/j.optlastec.2014.06.001](https://doi.org/10.1016/j.optlastec.2014.06.001).
- [14] Q. Fu, Y. Liu, Z. Liu, S. Li, and B. Guan, "High-accuracy SINS/LDV integration for long-distance land navigation," *IEEE/ASME Trans. Mechatronics*, vol. 23, no. 6, pp. 2952–2962, Dec. 2018, doi: [10.1109/TMECH.2018.2875151](https://doi.org/10.1109/TMECH.2018.2875151).
- [15] M. Wang, J. Cui, Y. Huang, W. Wu, and X. Du, "Schmidt ST-EKF for autonomous land vehicle SINS/ODO/LDV integrated navigation," *IEEE Trans. Instrum. Meas.*, vol. 70, pp. 1–9, 2021, doi: [10.1109/TIM.2021.3122530](https://doi.org/10.1109/TIM.2021.3122530).
- [16] Z. Xiang, Q. Wang, R. Huang, C. Xi, X. Nie, and J. Zhou, "In-motion initial alignment method for a laser Doppler velocimeter-aided strapdown inertial navigation system based on an adaptive unscented quaternion H-infinite filter," *Meas. Sci. Technol.*, vol. 33, no. 3, Mar. 2022, Art. no. 035001, doi: [10.1088/1361-6501/ac37e9](https://doi.org/10.1088/1361-6501/ac37e9).
- [17] Z. Xiang, Q. Wang, R. Huang, C. Xi, X. Nie, and J. Zhou, "A fast robust in-motion alignment method for laser Doppler velocimeter-aided strapdown inertial navigation system," *IEEE Sensors J.*, vol. 22, no. 17, pp. 17254–17265, Sep. 2022, doi: [10.1109/JSEN.2022.3191120](https://doi.org/10.1109/JSEN.2022.3191120).
- [18] Z. Xiang et al., "A SINS/GNSS/2D-LDV integrated navigation scheme for unmanned ground vehicles," *Meas. Sci. Technol.*, vol. 34, no. 12, Dec. 2023, Art. no. 125116, doi: [10.1088/1361-6501/acf2b4](https://doi.org/10.1088/1361-6501/acf2b4).
- [19] Z. Xiang, Q. Wang, R. Huang, S. Jin, X. Nie, and J. Zhou, "Online calibration method for pitch-independent laser Doppler velocimeter based on improved integrated navigation model," *IEEE Trans. Instrum. Meas.*, vol. 72, pp. 1–13, 2023, doi: [10.1109/TIM.2023.3315425](https://doi.org/10.1109/TIM.2023.3315425).
- [20] G. Yan, "Research on autonomous position and azimuth determining systems for land vehicles (in Chinese)," Ph.D. thesis, School Automat., 2006.
- [21] Y. Wu, M. Wu, X. Hu, and D. Hu, "Self-calibration for land navigation using inertial sensors and odometer: Observability analysis," in *Proc. AIAA Guid., Navigat., Control Conf.*, Aug. 2009, p. 5970, doi: [10.2514/6.2009-5970](https://doi.org/10.2514/6.2009-5970).
- [22] Q. Wang, X. Nie, C. Gao, J. Zhou, G. Wei, and X. Long, "Calibration of a three-dimensional laser Doppler velocimeter in a land integrated navigation system," *Appl. Opt.*, vol. 57, no. 29, p. 8566, Oct. 2018, doi: [10.1364/ao.57.008566](https://doi.org/10.1364/ao.57.008566).
- [23] L. Li et al., "Online calibration and compensation of total odometer error in an integrated system," *Measurement*, vol. 123, pp. 69–79, Jul. 2018, doi: [10.1016/j.measurement.2018.03.044](https://doi.org/10.1016/j.measurement.2018.03.044).
- [24] Q. Wang, C. Gao, J. Zhou, G. Wei, X. Nie, and X. Long, "Two-dimensional laser Doppler velocimeter and its integrated navigation with a strapdown inertial navigation system," *Appl. Opt.*, vol. 57, no. 13, p. 3334, May 2018, doi: [10.1364/ao.57.003334](https://doi.org/10.1364/ao.57.003334).
- [25] Y. Zhu, X. Wang, J. Zheng, H. Xiong, and Y. Zhao, "Using GPS time-differentiated carrier phase observations to calibrate LDV/INS integrated navigation systems," *IEEE Sensors J.*, vol. 20, no. 1, pp. 405–414, Jan. 2020, doi: [10.1109/JSEN.2019.2939551](https://doi.org/10.1109/JSEN.2019.2939551).
- [26] B. Xu, L. Wang, S. Li, and J. Zhang, "A novel calibration method of SINS/DVL integration navigation system based on quaternion," *IEEE Sensors J.*, vol. 20, no. 16, pp. 9567–9580, Aug. 2020, doi: [10.1109/JSEN.2020.2988500](https://doi.org/10.1109/JSEN.2020.2988500).
- [27] Q. Chen, Q. Zhang, and X. Niu, "Estimate the pitch and heading mounting angles of the IMU for land vehicular GNSS/INS integrated system," *IEEE Trans. Intell. Transp. Syst.*, vol. 22, no. 10, pp. 6503–6515, Oct. 2021, doi: [10.1109/TITS.2020.2993052](https://doi.org/10.1109/TITS.2020.2993052).
- [28] M. Yan, Z. Wang, and J. Zhang, "Online calibration of installation errors of SINS/OD integrated navigation system based on improved NHC," *IEEE Sensors J.*, vol. 22, no. 13, pp. 12602–12612, Jul. 2022, doi: [10.1109/JSEN.2022.3170707](https://doi.org/10.1109/JSEN.2022.3170707).
- [29] D. Wang, B. Wang, H. Huang, and Y. Yao, "Online calibration method of DVL error based on improved integrated navigation model," *IEEE Sensors J.*, vol. 22, no. 21, pp. 21082–21092, Nov. 2022, doi: [10.1109/JSEN.2022.3208327](https://doi.org/10.1109/JSEN.2022.3208327).
- [30] C. Gao, Q. Wang, G. Wei, and X. Long, "A highly accurate calibration method for terrestrial laser Doppler velocimeter," *IEEE Trans. Instrum. Meas.*, vol. 66, no. 8, pp. 1994–2003, Aug. 2017, doi: [10.1109/TIM.2017.2685078](https://doi.org/10.1109/TIM.2017.2685078).
- [31] C. Xi et al., "Online calibration technology for a one-dimensional laser Doppler velocimeter based on a strapdown inertial navigation system," *Appl. Opt.*, vol. 61, no. 5, p. 1229, Feb. 2022, doi: [10.1364/ao.446235](https://doi.org/10.1364/ao.446235).
- [32] W. Li, L. Zhang, F. Sun, L. Yang, M. Chen, and Y. Li, "Alignment calibration of IMU and Doppler sensors for precision INS/DVL integrated navigation," *Optik*, vol. 126, no. 23, pp. 3872–3876, Dec. 2015, doi: [10.1016/j.ijleo.2015.07.187](https://doi.org/10.1016/j.ijleo.2015.07.187).
- [33] X. Zhang, J. Yin, Z. Lin, and C. Zhang, "A positioning and orientation method based on the usage of INS and single-beam LiDAR," *Optik*, vol. 126, no. 22, pp. 3376–3381, Nov. 2015, doi: [10.1016/j.ijleo.2015.06.066](https://doi.org/10.1016/j.ijleo.2015.06.066).
- [34] Z. Xiang, Q. Wang, R. Huang, C. Xi, X. Nie, and J. Zhou, "Position observation-based calibration method for an LDV/SINS integrated navigation system," *Appl. Opt.*, vol. 60, no. 26, p. 7869, Sep. 2021, doi: [10.1364/ao.430866](https://doi.org/10.1364/ao.430866).
- [35] D. Wang, X. Xu, Y. Yang, and T. Zhang, "A quasi-Newton quaternions calibration method for DVL error aided GNSS," *IEEE Trans. Veh. Technol.*, vol. 70, no. 3, pp. 2465–2477, Mar. 2021, doi: [10.1109/TVT.2021.3059755](https://doi.org/10.1109/TVT.2021.3059755).
- [36] Q. Zhang, Y. Hu, S. Li, T. Zhang, and X. Niu, "Mounting parameter estimation from velocity vector observations for land vehicle navigation," *IEEE Trans. Ind. Electron.*, vol. 69, no. 4, pp. 4234–4244, Apr. 2022, doi: [10.1109/TIE.2021.3075883](https://doi.org/10.1109/TIE.2021.3075883).
- [37] R. N. Jazar, *Vehicle Dynamics*, vol. 24, no. 4, 2nd ed. New York, NY, USA: Springer, 2014.

**Zhiyi Xiang** received the M.E. degree from the College of Advanced Interdisciplinary Studies, National University of Defense Technology, Changsha, China, in 2021, where he is currently pursuing the Ph.D. degree.

His current research interest is SINS/LDV integrated navigation technology.

**Qi Wang** received the M.E. degree from the College of Optoelectronic Science and Engineering, National University of Defense Technology, Changsha, China, in 2013, and the Ph.D. degree from the College of Advanced Interdisciplinary Studies, National University of Defense Technology, in 2018.

He is currently an Associate Professor with the College of Advanced Interdisciplinary Studies, National University of Defense Technology. His research interests include laser Doppler velocimetry and SINS/LDV integrated navigation technology.

**Rong Huang** received the M.E. degree from the College of Advanced Interdisciplinary Studies, National University of Defense Technology, Changsha, China, in 2019, where she is currently pursuing the Ph.D. degree.

Her current research interests include laser Doppler velocimetry and SINS/LDV integrated navigation technology.

**Shilong Jin** received the M.E. and Ph.D. degrees from the College of Optoelectronic Science and Engineering, National University of Defense Technology, Changsha, China, in 1994 and 2006, respectively.

He is currently a Professor with the College of Advanced Interdisciplinary Studies, National University of Defense Technology. His interests include optoelectronic detection technology and inertial sensors and systems.

**Xiaoming Nie** received the M.E. and Ph.D. degrees from the College of Optoelectronic Science and Engineering, National University of Defense Technology, Changsha, China, in 2010 and 2014, respectively.

He is currently an Associate Professor with the College of Advanced Interdisciplinary Studies, National University of Defense Technology. His interests include optoelectronic velocimetry, laser Doppler velocimetry, and SINS/LDV integrated navigation technology.

**Jian Zhou** received the B.E. and Ph.D. degrees from the College of Optoelectronic Science and Engineering, National University of Defense Technology, Changsha, China, in 2006 and 2011, respectively.

He is currently an Associate Professor with the College of Advanced Interdisciplinary Studies, National University of Defense Technology. His research interests include optoelectronic velocimetry, laser Doppler velocimetry, and SINS/LDV integrated navigation technology.